




MICROSTRUCTURE AND MECHANICAL PROPERTIES OF THE INTERFACE OF ALUMINUM-BRASS BIMETALS PRODUCED VIA VERTICAL CENTRIFUGAL CASTING (VCC)

Morteza Gholami, Sina Ghaemi Khiavi , Ali Dehghani, Mehdi Akbarifar  and Mehdi Divandari 
 School of Metallurgy and Materials Engineering, Iran University of Science and Technology, Narmak 1684611314, Tehran, Iran

Copyright © 2023 American Foundry Society
<https://doi.org/10.1007/s40962-023-01096-5>

Abstract

Bimetal materials are composed of dissimilar metals, which are increasingly used to fabricate components that withstand harsh thermal and mechanical environments. In this work, aluminum-brass bimetallic hollow cylinders were produced using the vertical centrifugal casting process, and their interface was studied. Aluminum melt, with two different liquid-to-solid volume ratios of 1.5 and 2.5, was cast into brass hollow cylinders preheated to 100–400°C and rotated at 800, 1600, and 2000 rotation-per-minute. The sector-shaped samples were then studied using X-ray diffraction analysis, optical microscopy, scanning electron microscopy, and energy-dispersive X-ray spectroscopy. It was found that the interface consisted of three discernible layers. These included the chill zone ($Al_2Cu_5Zn_4 + Al_3Cu_3Zn$) near the brass side, platelet

precipitate zone (Al_2Cu precipitates scattered in $\alpha-Al$ solid solution matrix), and finally anomalous (or divorced) eutectic grains ($\alpha-Al/Al_3Cu$) near the aluminum side. Mechanical tests were carried out, in particular Brinell, Vickers and compression tests. The findings revealed that the adhesion of the interface was reduced by increasing the thickness of the interface. Fractography of fractured surfaces illustrated the presence of flat faces (Al_2Cu precipitates) locked together and deep depressions associated with cup-shaped dimples ($\alpha-Al/Al_3Cu$ eutectic).

Keywords: aluminum, brass, bimetal, metallurgical bond, centrifugal casting, interface

Introduction

Aluminum and its alloys are lightweight and have certain merits, such as high strength, formability, electrical and thermal conductivity, good corrosion resistance, and easy processing.^{1–3} Due to their outstanding thermal and electrical properties, copper alloys are also used in numerous industrial applications.^{4,5} For example, some brass alloys are used to produce electrical components, pipes, and fittings.⁵

As advanced functional materials, bimetallics are frequently and alternatively used in various fields to design engineering components with particular structural and functional properties.^{6,7} Bimetallic tubes are reliable for use in

challenging service conditions where the conventional heat transfer tubes cannot be responsive. A bimetallic aluminum and brass tube would be simultaneously favorable for corrosion resistance and good thermal and electrical conductivity. It is therefore appropriate for use in heat transfer systems and mechanical and electrical applications.⁸ Till now, various joining methods, including Diffusion Bonding,^{9–14} Friction Stir Welding (FSW),^{8,15,16} Ultrasonic Consolidation,¹⁷ Laser Welding,¹⁸ Brazing,¹⁹ and Accumulative Roll Bonding (ARB),²⁰ have been used to fabricate such bimetallics. In the mentioned joining methods, there is a limitation in the production of parts with arbitrary dimensions and complicated shapes.²¹ Compared to joining methods, compound casting can produce bimetallics at a low cost and with a more complex interface and good metallurgical bonding.²²

Compound casting is a process whereby the molten alloy is cast into or around a solid metal to form an

acceptable bond at the interface.^{23,24} A reaction zone is created at the interface of metals, which can be considered a transition layer containing intermetallic compounds upon which the joining performance depends.^{25,26} Crystal nucleation at the interface is related to heat transfer between the melt and solid metal. It therefore controls the microstructure formed after the solidification process.²⁷ Solidification is a short and dynamic process with no thermodynamic equilibrium.²⁸ Some uncontrollable factors, such as gas entrapment and surface roughness, can mainly affect heat transfer.²⁹ Production of parts using this process is easier with less time-consuming, low operating cost, mass savings, design flexibility, excellent performance, and high production efficiency.^{2,30,31} In this process, the melt-to-solid volume ratio and the preheat temperature are the most critical parameters affecting the properties of the produced part.³⁰

The vertical centrifugal casting (VCC) method is widely used to produce thin-walled or complex-shaped castings that are increasingly used in the aerospace industry.³² The centrifugal casting method uses centrifugal force and can be performed both horizontally and vertically.^{33,34} The horizontal mode of the process is typically used to produce pipes, tubes, cylinders, and the same.³³ Since the entrance length of the melt in the vertical mode is shorter than that of the horizontal mode, the molten alloy can be poured directly into a rotating mold. Pouring temperature and liquid-to-solid volume ratio are more easily controlled in vertical mode casting.

In this study, the VCC method was used to produce aluminum-brass bimetal hollow cylinders. Aluminum melt in two different liquid-to-solid volume ratios of 1.5 and 2.5 are cast into 100–400 °C preheated brass hollow cylinder, which is rotated at 800, 1600, and 2000 rotation-per-minute (rpm), and the interface is characterized.

Materials and Methods

Materials

The chemical composition of aluminum ingots used in this research is given in Table 1. A commercial CuZn35 brass sheet with the specific chemical composition shown in Table 2 was also used to produce hollow brass cylinders.

Table 1. Chemical Composition (wt%) of Aluminum Ingots

Material	Si	Fe	Mg	Mn	Al
Al ingot	0.08	0.064	0.027	0.006	Bal.

Table 2. Chemical Composition (wt%) of CuZn35 Brass Sheet

Material	Zn	Ni	Sn	Fe	Pb	Al	Cu
CuZn35	35	0.3	0.1	0.05	0.05	0.02	Bal.

The preparation of the hollow brass cylinder was accomplished in two steps. At first, the CuZn35 sheet was cut out to 265 × 40 × 3 mm³ dimensions and then rolled into a cylindrical shape with external and internal diameters of 84 and 78 mm and a height of 40 mm. The seam was fastened with asbestos and steel wires (Figure 1). Silicon carbide emery paper up to 2000 grit and acetone solution were used to eliminate any oxides or dirt from the hollow brass cylinder surfaces.

Equipment

Aluminum ingots were melted at 700°C using a resistance furnace. According to liquid-to-solid (L/S) ratios of 1.5 and 2.5, the amount of aluminum poured was 243 and 405 gr, respectively. A given melt volume was poured into the rotating hollow cylinder inserted vertically into the casting machine. According to the L/S volume ratios of 1.5 and 2, theoretically, bimetallic hollow cylinders with inner diameters of approximately 68 and 64 mm and outer diameters of 84 mm were produced, respectively. A schematic of the casting machine components used in this research is shown in Figure 2. Once the casting process was completed, the bimetallic hollow cylinders were cut out into sector shapes (Figure 3). Next, the cross-section area of the sector-shaped samples was subjected to preparation treatments, including sandpapering and polishing with 0.3 μm alumina particles. Microstructure evaluations were conducted using optical microscopy (Olympus BX51M Model) and scanning electron microscopy (SEM). X-ray diffraction analysis (XRD) and energy dispersive spectroscopy (EDS) were used to determine the chemical composition of the phases. The Wolpert device was used to estimate macro hardness, while the MXT device was used to measure phase hardness. Adhesive bond strength was determined using a Schenck-Trebel compression device, and fractured surfaces were analyzed by SEM.

Casting Conditions

In this research, three effective parameters, including rotation speed (rpm), liquid-to-solid ratio (L/S), and brass hollow cylinder preheat temperature (°C), were investigated. Values of 800, 1600, and 2000 rpm were chosen for the rotational speed. Values of 1.5 and 2.5 were selected to investigate the effect of liquid-to-solid ratio (L/S) on interface formation. Additionally, temperatures of 100,



Fig. 1. The preparation process of a brass hollow cylinder; (a) Brass sheet cut out to $265 \times 40 \times 3 \text{ mm}^3$ dimensions and (b) Brass sheet formed into a cylindrical shape and closed using asbestos and steel wires.

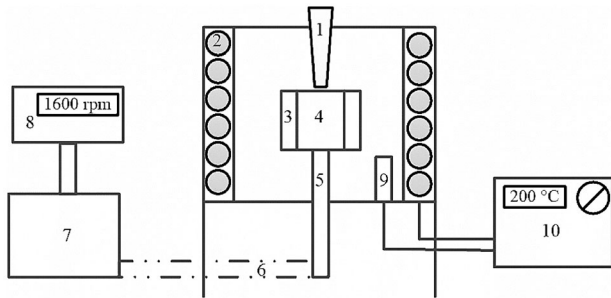


Fig. 2. Schematic representation of vertical centrifugal casting (VCC) machine; (1) sprue (2) heating element (3) brass hollow cylinder (4) die cavity (5) shaft (6) bet pulley (7) electromotor (8) inverter (9) thermometer attached to the heating generator and (10) heating generator and controller.

200, 300 and 400 °C were selected to examine the effect of preheat temperature on interface formation. In total, 24 samples were manufactured and analyzed to investigate three important parameters. The casting conditions of the samples are given in Table 3. The direction of rotation in this work was counter-clockwise. Hence, the melt flowed in the opposite direction, rose, and touched the upper areas of the hollow cylinder, and then it glided down so that an irregular tube was formed. The hot flowing melt dissolved

the brass surface; thus, a triple solution of Al, Cu, and Zn elements was created. The first areas touched by the melt were the most preferential sites for metallurgical bonding due to the melt's higher heat content in the early stages. The metallurgical joints in the samples produced during this research could be attributed to a particular dissolution condition created by the involved multiple mechanical forces and also likely solid diffusion.

Results and Discussions

Bond Formation

Figure 4 shows a sector of sample 2. It is evident that an integrated metallurgical bond is not formed throughout the interface, and defective zones are detected. The resultant of the centrifuge and Coriolis forces not only causes the melt to rise in the hollow cylinder but also leads to the rupture of the surface oxide layer on the melt. In fact, these forces break the formerly formed-oxide film on the melt so that the solid surface, i.e., the brass part efficiently wetted by the melt; thereby, a metallurgical bond has been obtained. According to Pan et al.,³⁵ high strength bond is dependent on the breakage of the surface oxide film.

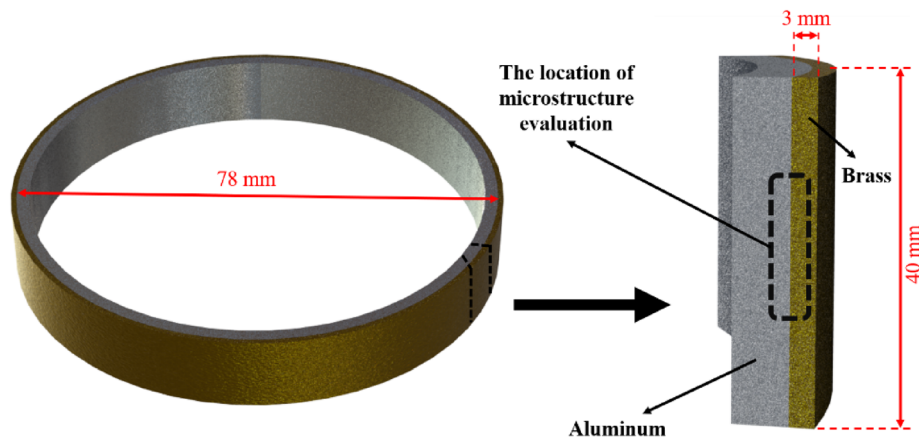


Fig. 3. Preparation of sector-shaped samples from the cast samples for metallographic observations.

Table 3. Cast Samples at 700°C Pouring Temperature

Sample no.	Rotational speed (rpm)	Liquid-to-Solid ratio (L/S)	Hollow cylinder preheated temperature (°C)	Interface thickness (mm)
1	800	1.5	100	1.21
2	1600			0.83
3	2000			0.489
4	800	2.5		1.48
5	1600			1.02
6	2000			0.7
7	800			1.78
8	1600	1.5	200	1.5
9	2000			0.78
10	800			1.9
11	1600	2.5		1.7
12	2000			0.84
13	800			2.13
14	1600	1.5		1.8
15	2000		300	0.88
16	800			2.21
17	1600	2.5		1.85
18	2000			1.13
19	800			2.84
20	1600	1.5		2.01
21	2000		400	1.4
22	800			3.11
23	1600	2.5		2.12
24	2000			1.63

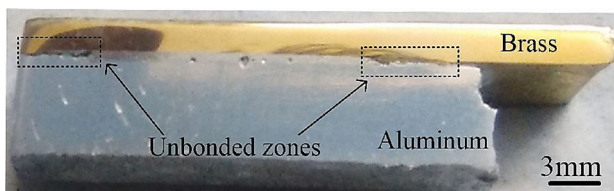


Fig. 4. Sector representation of sample 2 showing bonded and unbonded.

Interface Characterization

Figure 5 shows the interface of sample 5, which is composed of three distinct layers, including the chill zone (first layer) near the brass side, the platelet precipitates zone (second layer), and the anomalous (or divorced) eutectic zone (third layer) near the aluminum side.

Figure 6 demonstrates the chill zone (Zone 1) composed of two continuous layers near the brass side. According to EDS analysis (Table 4), these layers are $Al_2Cu_5Zn_4$ and

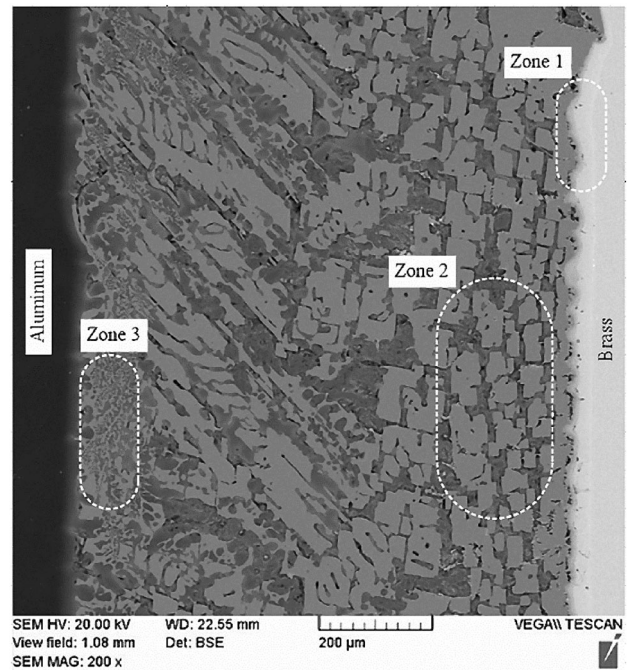


Fig. 5. SEM micrograph of the interface of sample 5 shows three distinct layers formed.

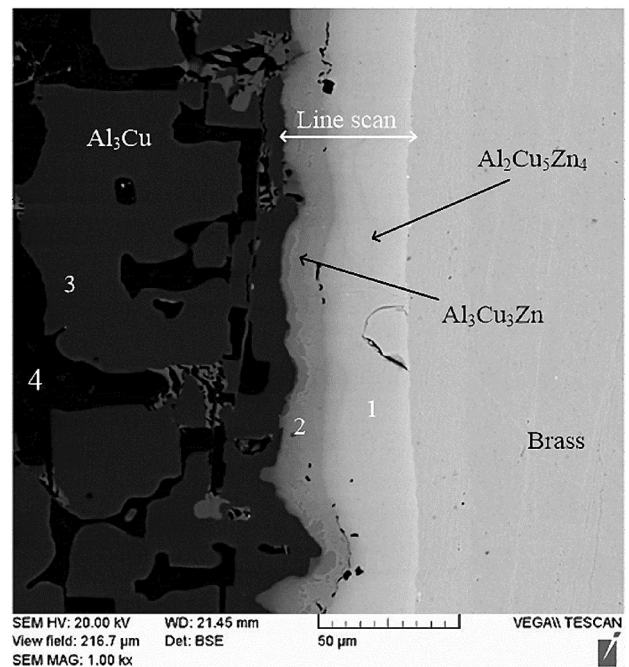


Fig. 6. SEM micrograph of the chill zone of sample 1.

Al_3Cu_3Zn , respectively. According to Raghavan,³⁶ the only ternary intermetallic compound in the Al-Cu-Zn system is Al_4Cu_3Zn , it is therefore possible to deduce that the solid diffusion has occurred after the solidification process. Zn's uphill diffusion may be related to the Kirkendall effect (Figure 7). Moreover, literature results^{11,13,37} show that the Zn-rich side of the interface near the brass can indicate this element's uphill diffusion.

Table 4. EDS Results (Atomic %) of Points are Shown in Figures 6, 9, and 18

Point	Element composition (Atomic %)			Suggested compound
	Zn	Cu	Al	
1	36.94	45.08	17.99	$\text{Al}_2\text{Cu}_5\text{Zn}_4$
2	14.23	41.8	43.98	$\text{Al}_3\text{Cu}_3\text{Zn}$
3	1.47	25.35	73.18	Al_3Cu
4	11.28	2.86	85.86	Al_{11}Zn
5	–	25.38	74.62	Al_3Cu
6	8.07	2.39	89.54	Al_{11}Zn
7	0.99	23.36	75.65	Al_3Cu

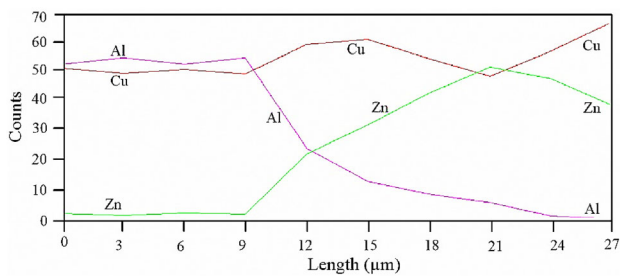


Fig. 7. Line scan of the location marked in Figure 6 shows up-hill diffusion of Zink (Kirkendall effect).³⁸

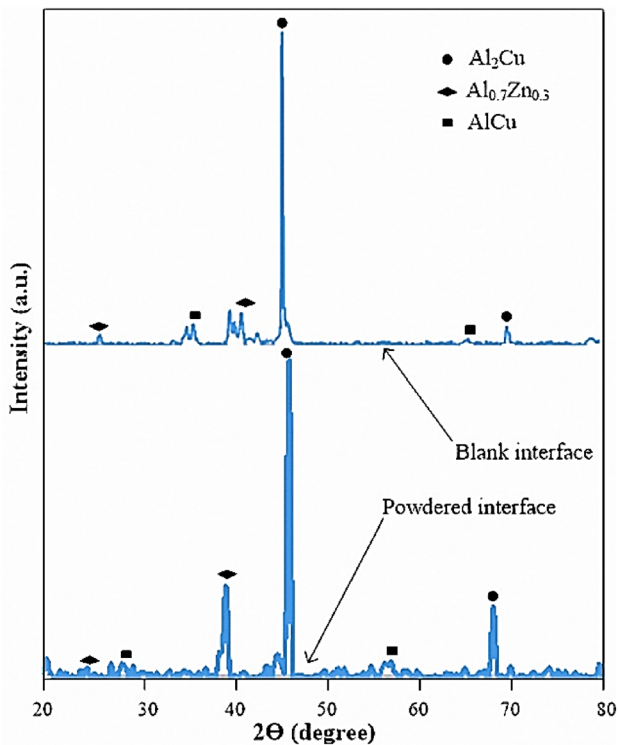


Fig. 8. X-ray diffraction (XRD) analysis of the interface of sample 7 at blanked, and powdered states.

As shown in Figure 5, the platelet precipitate zone is a significant part of the interface. Figure 8 displays the interface's X-ray diffraction (XRD) pattern. It is obvious that the Al_2Cu phase is dominant. According to EDS results (Table 4), this phase has been recognized as the Al_3Cu phase. As a matter of fact, non-equilibrium conditions and high cooling rates cause this phenomenon so, the fundamental phase in this zone is the same Al_2Cu phase. Previous reports by Biswas et al.³⁹ and Shoilock et al.⁴⁰ show that rapid solidification under unstable conditions leads to this behavior. The solid solubility of zinc in aluminum is much more than vice-versa,⁴¹ so the interface includes an Al-Zn solid solution matrix. According to Springer et al.,⁴² the Al-Zn liquid zone guarantees bond formation between melt and solid layers.

Figure 9 represents the third layer composed of $\alpha\text{-Al}/\text{Al}_3\text{Cu}$ anomalous (or divorced) eutectic grains. Non-isothermal eutectic solidification causes such behavior.^{43,44}

Heat Capacity Effects

In this research, the significant effect of heat capacity is on the first layer, i.e., the chill zone. Figure 10a and b demonstrates variations in the layer thickness of the $\text{Al}_2\text{Cu}_5\text{Zn}_4$ and $\text{Al}_3\text{Cu}_3\text{Zn}$ with respect to the hollow cylinder preheat temperature. $\text{Al}_2\text{Cu}_5\text{Zn}_4$ and $\text{Al}_3\text{Cu}_3\text{Zn}$ thickness ranges were measured at 46–82 μm and 14–26 μm , respectively. As mentioned earlier, the uphill diffusion of Zn causes such behavior that higher heat capacity exacerbates this phenomenon. According to Springer et al.,⁴² the presence of Zn

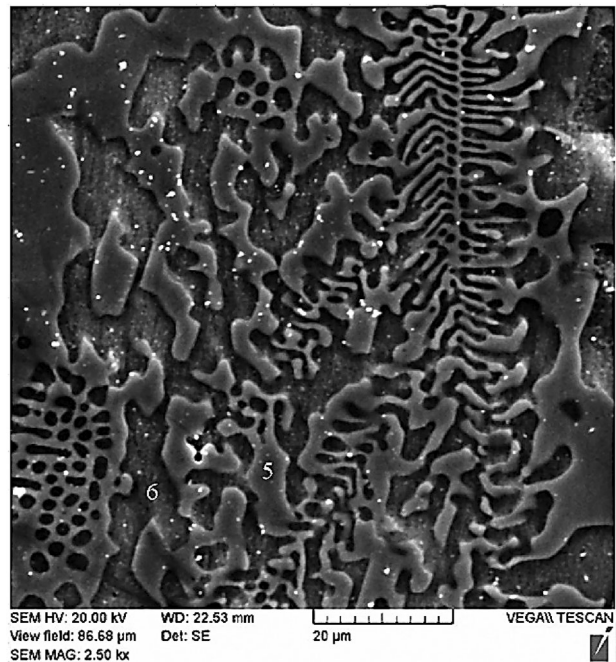


Fig. 9. SEM micrograph of $\alpha\text{-Al}/\text{Al}_3\text{Cu}$ anomalous (or divorced) eutectic microstructure of sample 15.

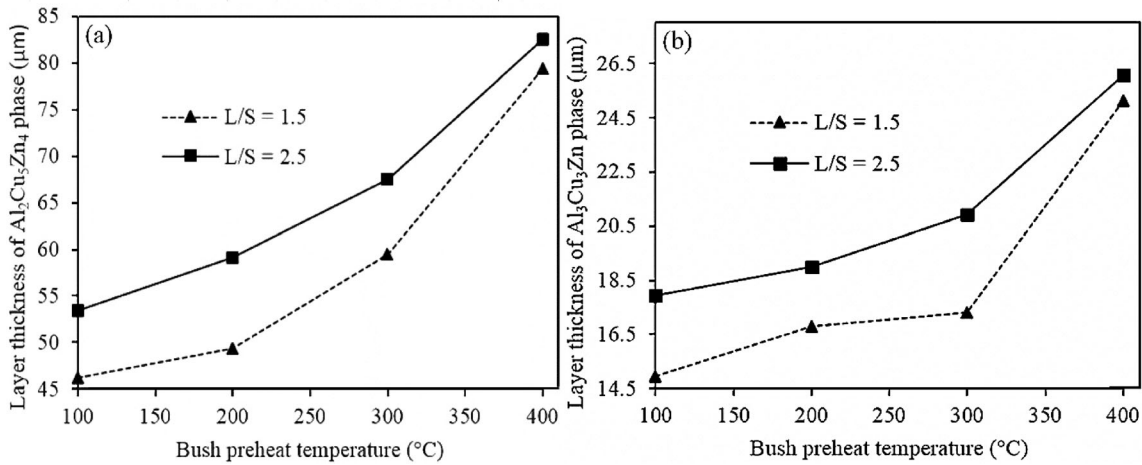


Fig. 10. Variations of the layer thickness of (a) $Al_2Cu_5Zn_4$ and (b) Al_3Cu_3Zn phases versus hollow cylinder preheat temperature at constant 800 rpm rotation speed and variable L/S ratios.³⁸

associated with structural vacancies facilitates the inter-diffusion of elements. According to Timisit,¹¹ the heat capacity caused by liquid-to-solid ratios provides the driving force for activating the atoms involved in a system (here are Al, Cu, and Zn). Additionally, the dissolution and growth of the reaction layer is activated by heat, which is discussed by Viala et al.⁴⁵

Figure 11 displays the brass vicinity interface of sample 23. Heat capacity increment not only widens the chill zone but also creates some thermal cracks in this zone. Aguado et al.⁴⁶ have related these crack formations to induce thermal shear stress release. In other words, the high temperature of the interface near the brass side (due to the direction of the heat transfer) and involved contraction stresses are the driving forces of such cracks. Moreover, the non-uniform distribution of heat at the brass surface facilitates the formation of these cracks.

Centrifuge Field Effects

Platelet Precipitates Zone

Figure 12 demonstrates the thickness of the interface which is decreased by increasing the rotational speed. As a matter

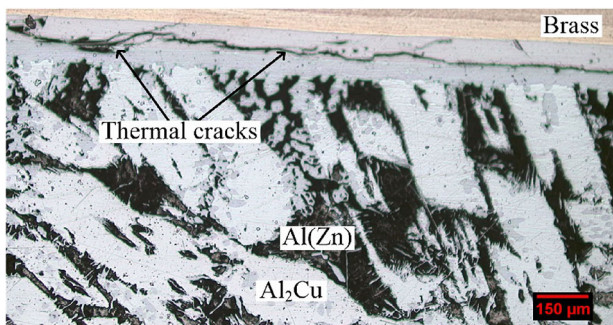


Fig. 11. Optical representative of sample 23 showing thermal cracks at the chill zone.

of fact, a higher rotation speed causes an increase in the cooling rate and reduces the diffusion period. On the other hand, higher liquid-to-solid ratios can facilitate elemental diffusion, and as a result, the interfacial region has been widened, which is discussed by Xiong et al.⁴⁷

The average size of platelet precipitates for samples 1–24 are, respectively, measured as 3199.14, 1656.95, 1303.03,

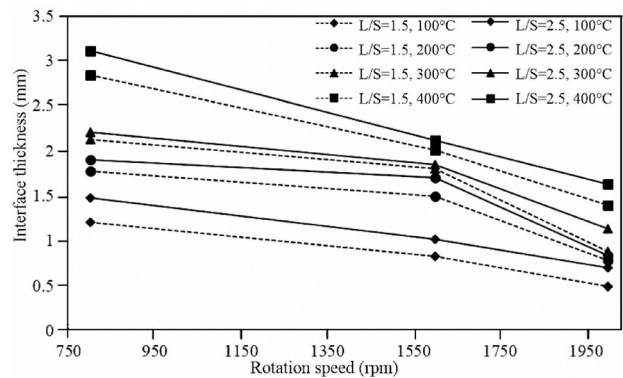


Fig. 12. Variation of the interface thickness versus rotation speed.

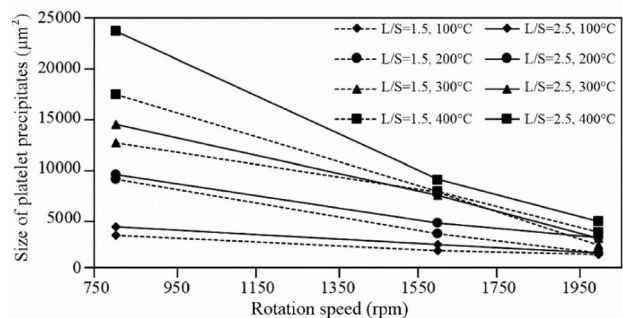


Fig. 13. Variety of the platelet precipitate sizes versus rotation speed.

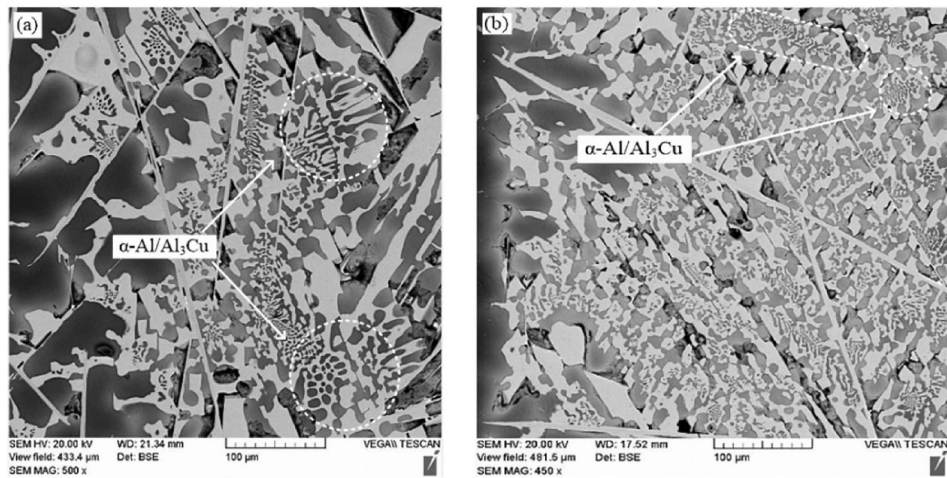


Fig. 14. SEM micrographs of anomalous (or divorced) eutectic grains of samples of (a) 4 in magnification of 500x and (b) 6 in magnification of 450x.

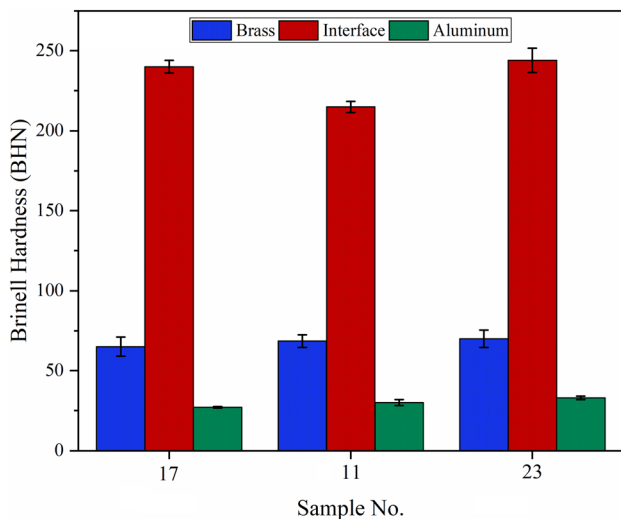


Fig. 15. Brinell test results of samples 11, 17, and 23.³⁸

4067.65, 2310.3, 1430.77, 8845.31, 3351.49, 1438.4, 9276.96, 4479.33, 2942.25, 12463.08, 7487.42, 2212.54, 14289.16, 7217.45, 2923.16, 17322.56, 7615.27, 3492.35, 23607.3, 8793.54, and 4621.77 μm^2 . It can be seen that the largest one belongs to the broadest interface (sample 22), and the smallest one belongs to the thinnest interface (sample 3). Figure 13 represents the variation of platelet precipitate size and rotation speed. It is obvious that the rotation speed increment is responsible for modifying the solidified microstructure. In other words, rotation speed increment increases the cooling rate and reduces the solidification time by promoting more nuclei into the melt. According to Ghoncheh et al.,⁴⁸ the diffusion process decreases while the mobility of atoms increases at the solid/liquid interface. Therefore, the centrifugal field reduces intermetallic compounds' nucleation and growth temperature, so there is insufficient time for atom diffusion and the coarsening of intermetallic compounds.

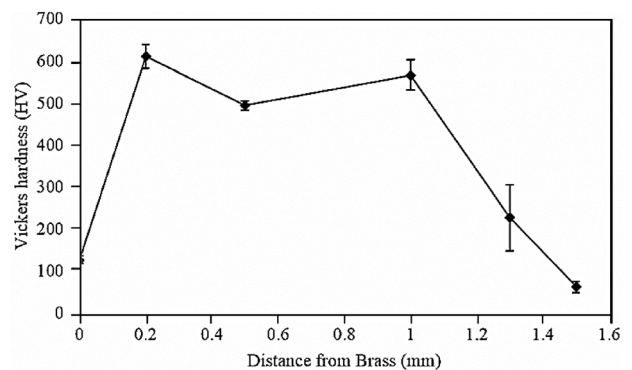


Fig. 16. Micro-hardness profile along with the aluminum-brass interface.³⁸

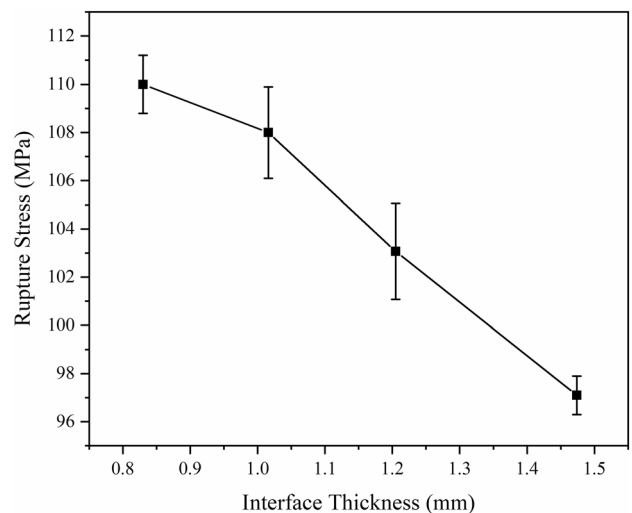


Fig. 17. Variation of interface rupture stress versus interface thickness.⁵³

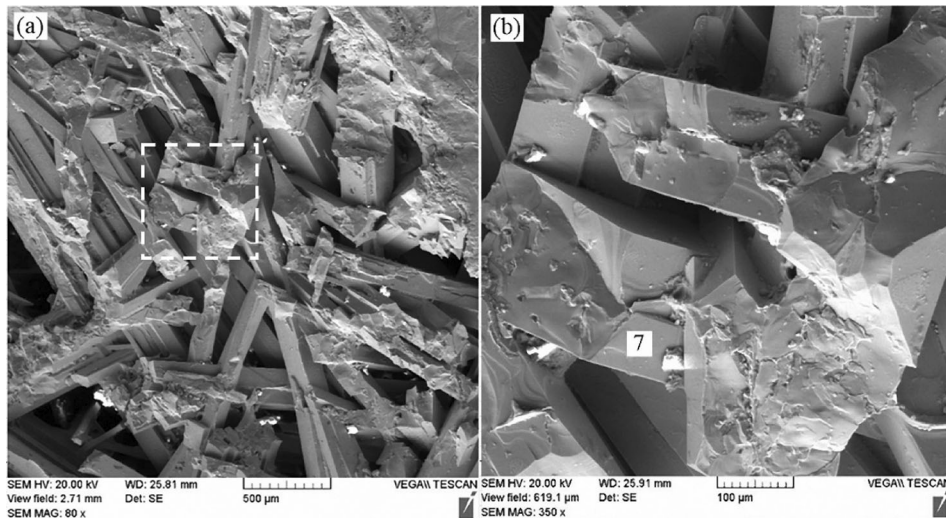


Fig. 18. SEM micrographs of platelet precipitates locked together at the fractured surfaces near the aluminum side in magnification of (a) 80x and (b) 350x.

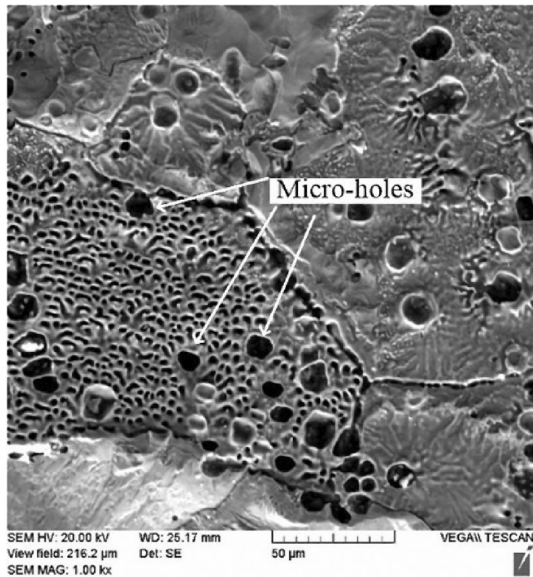


Fig. 19. SEM micrograph of micro-holes at the fractured surface near the aluminum side in magnification of 1000x.

Anomalous (or Divorced) Eutectic Zone

Figure 14 displays the anomalous (or divorced) eutectic zone of samples 4 and 6. It is evident that microstructure modification has been created by increasing in the speed of rotation. In fact, thermal under-cooling (cooling effect) and constitutional under-cooling (promoting more nuclei into the melt) have intensified due to increased rotation speed. In other words, melt agitation forces the liquid to float and prevents grain growth. According to Xiong et al.,⁴⁹ melt agitation increases constitutional under-cooling by accelerating thermal convection and solute diffusion.

Mechanical Analysis of the Interface

Hardness Tests

Two hardness tests are accomplished in this work, including Brinell and Vickers. Figure 15 demonstrates the result of the Brinell test for samples 11, 17, and 23. Intermetallic compounds present at the interface compared to base metals (aluminum and brass) cause such differences in the measured data. In fact, hardness values are reduced from outward to inward at the centrifuge field, which is discussed by Sarkar et al.⁵⁰

Figure 16 represents Vickers hardness results. Hardness values drop steadily toward the aluminum side of the interface. The highest microhardness value (equal to 610 VHN) belongs to the $Al_2Cu_5Zn_4$ phase. The platelet precipitates zone containing the Al_2Cu phase has a 565 VHN microhardness value. Due to the introduction of centrifugal force to the formed phases, the presence of phases with a high density like $Al_2Cu_5Zn_4$ in the outer part and phases with a low density like Al_2Cu in the inner part of the bimetallic interface is more probable.

Compression Test

Figure 17 demonstrates the variation of the rupture stress in relation to the interface thickness for samples 4, 10, 16, and 22. As can be seen, the adhesion of the interface is reduced by increasing the thickness of the interface. It is evident that the brittleness of the intermetallic compounds causes such behavior. According to Abbasi et al.,⁵¹ the intermetallic compound has a critical size over which the bond strength is sharply reduced.

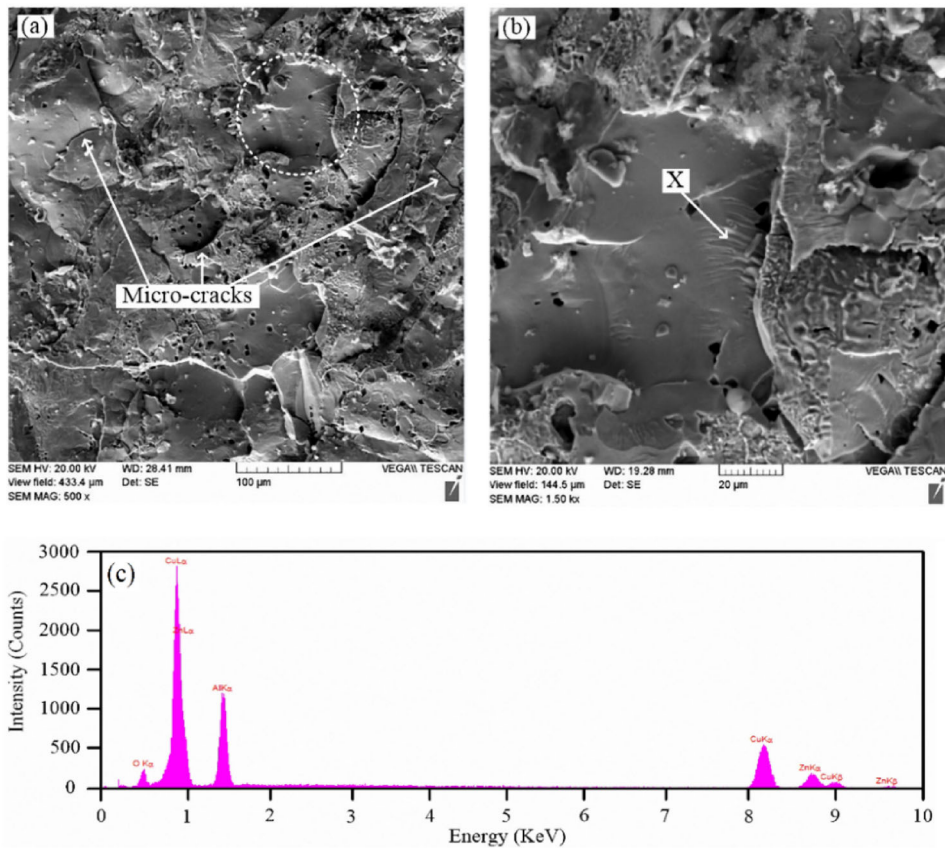


Fig. 20. SEM micrographs of (a) micro-cracks in magnification of 500x, (b) oxidized surface in magnification of 1500x, and (c) EDS analysis of marked point on the fractured surface near brass side.

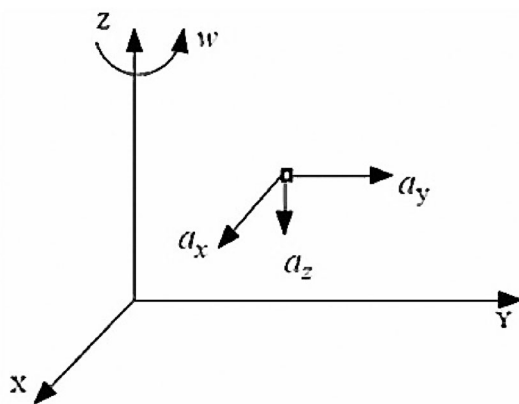


Fig. 21. Cell accelerations in different directions.

Finally, the fractured surfaces were characterized. Fractography of the fractured surface close to the aluminum side shows flat faces locked together (Figure 18a and b). EDS results determined that these flat faces are the same platelet precipitates responsible for brittle fractures. According to Lawson and Kerr,⁵² planar propagation of the brittle fracture mode represents a uniform failure of inter-metallic compounds.

Deep depressions associated with cup-shaped dimples, illustrated in Figure 19, represent ductile fracture. Micro-holes are created and grown at the secondary phase (Al_3Cu in this work) until the walls between these micro-holes begin to break, which Beachem discussed.⁵⁴ Therefore, it is sufficient to state that ductile behavior depends on this microstructure. Figure 20a illustrates some micro-cracks created close to the brass side. According to Gilbert et al.⁵⁵, these micro-cracks are observed in microstructures subjected to compression testing. Oxidized surfaces are also identified on this side (Figure 20b and c).

Conclusions

Aluminum-brass bimetal was successfully produced via vertical centrifugal casting as a compound casting process. The findings of this research can be summed up as follows:

The metallurgical joint in this research was probably due to a particular dissolving condition provided by multiple mechanical forces involved and possible solid diffusion at the end of the solidification process.

The resulting interface was composed of three distinct layers, including the chill zone (first layer) near the brass

side, the platelet precipitates zone (second layer), and the anomalous (or divorced) eutectic zone (third layer) near the aluminum side.

The platelet precipitates zone was the main part of the interface. The broadest interface (equal to 3.11 mm) contained the largest Al₂Cu precipitates (23607.3 μm²). On the other hand, the thinnest interface (equal to 0.489 mm) contained the smallest Al₂Cu precipitates (equal to 1303.03 μm²).

Thermal under-cooling (cooling effect) and constitutional under-cooling (promoting more nuclei into the melt) were intensified due to the increased rotation speed so that microstructure modification occurred.

The hardness values were reduced from the outside to the inside to the field of the centrifuge. Interfacial adhesion was reduced by increasing the thickness of the interface due to the brittleness of the intermetallic compounds.

Fractography of the fractured surfaces represented flat faces locked together. EDS results determined that these flat faces were the same platelet precipitates that were responsible for brittle fracture. Deep depressions associated with cup-shaped dimples (Al₃Cu eutectic phase) were also responsible for ductile fracture.

Acknowledgments

We would like to express our gratitude to the members of Dr. M. Divandari's Lab. (Porous and Lattice Materials Laboratory of Iran University of Science and Technology).

Author contribution All authors contributed to the study's conception and design. Material preparation, data collection, and analysis were performed by [MG], [AD], and [MA]. The first draft of the manuscript was written by [MG] and review and editing were performed by [SGK]. Also, this research was under the supervision of [MD]. All authors commented on previous versions of the manuscript. All authors read and approved the final manuscript.

Funding

The authors declare that no funds, grants, or other support were received during the preparation of this manuscript.

Data Availability

The authors declare that there are no restrictions on the availability of data and material.

Conflict of interest The authors declare no competing interests.

Appendix

Governing equations

Forces analysis

Mold rotation around its centerline not only causes a centrifuge field but also intensifies the gravitational force, which is exposed on both filling and solidifying liquid metal. By supposing the liquid metal to behave like an incompressible Newtonian fluid, the governing mass and momentum equations can be derived using the Navier-Stokes equations:

$$F - \frac{1}{\rho} \nabla P + \mu \Delta U = \frac{\partial U}{\partial t} + (U \cdot \nabla) U \quad \text{Eqn. a1}$$

$$\nabla \cdot U = 0 \quad \text{Eqn. a2}$$

where F , ρ , P , μ , U $\langle u, v, w \rangle$, and t represent, respectively, acceleration, fluid density, pressure, viscosity, velocity vector in Cartesian coordinates, and time. The acceleration components are affected by the centrifuge and Coriolis forces (Fig. 21). They are applied in three different directions a_x , a_y , and a_z :

$$a_x = \omega^2 x + 2\omega v_r \quad \text{Eqn. a3}$$

$$a_y = \omega^2 y - 2\omega u_r \quad \text{Eqn. a4}$$

$$a_z = g \quad \text{Eqn. a5}$$

where ω , u_r , v_r , and g , respectively, relate to angular velocity, velocities relative to X and Y directions, and gravity acceleration.^{56,57} Moreover, centripetal acceleration is also involved in this process. The acceleration responsible for uniform circular motion is called centripetal acceleration, and its value can be calculated by:

$$a = \frac{s^2}{r} \quad \text{Eqn. a6}$$

In which r is the mold radius and s represents a tangential velocity of a particle.⁵⁸

Heat transfer

The thermal energy transfer equation in the VCC process can be derived as follows:

$$\frac{\partial T}{\partial t} + \nabla \cdot (vT) = \alpha \nabla^2 T + \frac{h}{c_p} \frac{\partial f_s}{\partial t} \quad \text{Eqn. a7}$$

where T and f_s represent temperature and solidified phase fraction, respectively; α also indicates thermal diffusivity and equals to:

$$\alpha = \frac{\lambda}{c_p \rho_L} \quad \text{Eqn. a8}$$

In which λ , ρ_L , h , and c_p are thermal conductivity, fluid density, latent heat, and specific heat, respectively.³² Actually, heat transfer increment at the centrifuge field alleviates the temperature gradient and accelerates the solidification rate so that directional solidification occurs.⁵⁹

Solidification

Mold rotation improves alloy texture and reduces defects by pressurizing the melt.⁶⁰ Generally, rapid heat extraction at the centrifuge field promotes directional solidification.⁵⁹ The continuity and Navier-Stokes equations in a control volume of a fluid with v_x , v_y , and v_z velocity components are as follows:

$$\frac{\partial v_x}{\partial x} + \frac{\partial v_y}{\partial y} + \frac{\partial v_z}{\partial z} = \nabla v = 0 \quad \text{Eqn. a9}$$

$$\rho \frac{dv}{dt} = -\nabla p + \eta \nabla^2 v + \rho g \quad \text{Eqn. a10}$$

Equation (10) can be rewritten for cylindrical coordinates:

$$\begin{aligned} \rho \left(\frac{\partial v_x}{\partial t} + v_x \frac{\partial v_x}{\partial x} + v_y \frac{\partial v_y}{\partial y} + v_z \frac{\partial v_z}{\partial z} \right) &= -\frac{\partial p}{\partial x} + \eta \nabla^2 v + \rho g_x \\ \rho \left(\frac{\partial v_y}{\partial t} + v_x \frac{\partial v_x}{\partial x} + v_y \frac{\partial v_y}{\partial y} + v_z \frac{\partial v_z}{\partial z} \right) &= -\frac{\partial p}{\partial y} + \eta \nabla^2 v + \rho g_y \\ \rho \left(\frac{\partial v_z}{\partial t} + v_x \frac{\partial v_x}{\partial x} + v_y \frac{\partial v_y}{\partial y} + v_z \frac{\partial v_z}{\partial z} \right) &= -\frac{\partial p}{\partial z} + \eta \nabla^2 v + \rho g_z \end{aligned} \quad \text{Eqn. a11}$$

where ρ , p , $\eta \nabla^2 v$, and ρg are, respectively, stood for density, pressure, viscous force, and gravitational force.^{60,61}

REFERENCES

1. M. Akbari, R.A. Behnagh, Dissimilar friction-stir lap joining of 5083 aluminum alloy to CuZn34 brass. *Metall. Mater. Trans. B* **43**, 1177–1186 (2012). <https://doi.org/10.1007/s11663-012-9682-y>
2. M.A. Ali, M. Jahanzaib, A. Wasim et al., Evaluating the effects of as-casted and aged overcasting of Al-Al joints. *Int. J. Adv. Manuf. Technol.* **96**, 1377–1392 (2018). <https://doi.org/10.1007/s00170-018-1682-x>
3. G. Li, W. Jiang, F. Guan et al., Microstructure, mechanical properties and corrosion resistance of A356 aluminum/AZ91D magnesium bimetal prepared by a compound casting combined with a novel Ni-Cu composite interlayer. *J. Mater. Process. Technol.* **288**, 116874 (2021). <https://doi.org/10.1016/j.jmatprotec.2020.116874>
4. G. Zare, M. Divandari, H. Arabi, Investigation on interface of Al/Cu couples in compound casting.

5. Mater. Sci. Technol. **29**, 190–196 (2013). <https://doi.org/10.1179/1743284712Y.0000000096>
6. H.R. Zareie Rajani, A. Esmaili, M. Mohammadi et al., The role of metal-matrix composite development during friction stir welding of aluminum to brass in weld characteristics. *J. Mater. Eng. Perform.* **21**(11), 2429–2437 (2012). <https://doi.org/10.1007/s11665-012-0178-3>
7. S. Palraj, G. Subramanian, S. Palanichamy, Galvanic interactions of aluminium 3004 and brass in tropical marine atmosphere. *J. Marine Sci. Appl.* **13**, 455–461 (2014). <https://doi.org/10.1007/s11804-014-1274-6>
8. J. Xu, X. Gao, Z. Jiang et al., Microstructure and hot deformation behaviour of high-carbon steel/low-carbon steel bimetal prepared by centrifugal composite casting. *Int. J. Adv. Manuf. Technol.* **86**, 817–827 (2016). <https://doi.org/10.1007/s00170-015-8232-6>
9. A. Esmaili, M.K. Besharati Givi, H.R. Zareie Rajani, A metallurgical and mechanical study on dissimilar Friction stir welding of aluminum 1050 to brass (CuZn30). *Mater. Sci. Eng. A* **528**, 7093–7102 (2011). <https://doi.org/10.1016/j.msea.2011.06.004>
10. A.A. Ershov, T.A. Sycheva, P.F. Zasoukha, Reactional diffusion in three-layer aluminum-brass bimetal. *Metal Sci. Heat Treat.* (1997). <https://doi.org/10.1007/BF00703007>
11. Y. Fouad, Characterization of High strength stainless Steel/Al/Brass composite tri-layered clad. *Trans. Indian Inst. Met.* (2014). <https://doi.org/10.1007/s12666-014-0419-2>
12. R.S. Timsit, Intermetallics growth at Al α -brass interfaces. *Acta Metall.* **33**, 97–104 (1985). [https://doi.org/10.1016/0001-6160\(85\)90223-8](https://doi.org/10.1016/0001-6160(85)90223-8)
13. R.S. Timsit, Electrical instabilities in stationary contacts: Al/Al and Al/Brass junctions. In: *Electrical Contacts; Proceedings of the Thirty Fourth Meeting of the IEEE Holm Conference*, (1988). <https://doi.org/10.1109/HOLM.1988.16111>
14. R.S. Timisit, Interdiffusion at Bimetallic Electrical Interfaces. *IEEE Trans. Compon. Hybrids Manuf. Technol.* (1986). <https://doi.org/10.1109/TCHMT.1986.1136613>
15. R.S. Timisit, Electrical instabilities in stationary contacts: Al-Plated-brass junctions. *IEEE Trans. Compon. Hybrids Manuf. Technol.* (1988). <https://doi.org/10.1109/33.2961>
16. A. Esmaili, H.R. Zareie Rajani, M. Sharbati et al., The role of rotation speed on intermetallic compounds formation and mechanical behavior of friction stir welded brass/aluminum 1050 couple. *Intermetallics* **19**, 1711–1719 (2011). <https://doi.org/10.1016/j.intermet.2011.07.006>
17. M. Shojaeefard, M. Akbari, M. Tahani et al., Sensitivity analysis of the artificial neural network outputs in friction stir lap joining of aluminum to brass. *Adv. Mater. Sci. Eng.* (2013). <https://doi.org/10.1155/2013/574914>

17. G.D. Janaki Ram, C. Robinson, Y. Yang et al., Use of ultrasonic consolidation for fabrication of multi-material structures. *Rapid Prototyp. J.* (2007). <https://doi.org/10.1108/13552540710776179>
18. X. Qi, G. Song, Interfacial structure of the joints between magnesium alloy and mild steel with nickel as interlayer by hybrid laser-TIG welding. *Mater. Des.* **31**, 605–609 (2010). <https://doi.org/10.1016/j.matdes.2009.06.043>
19. L. Peng, L. Yajiang, W. Juan et al., Vacuum brazing technology and microstructure near the interface of Al/18-8 stainless steel. *Mater. Res. Bull.* **38**, 1493–1499 (2003). [https://doi.org/10.1016/S0025-5408\(03\)00176-4](https://doi.org/10.1016/S0025-5408(03)00176-4)
20. J.G.Frydendahl, Multilayered Composites of AA3103 and Cu produced by accumulative roll bonding (ARB). (2012)
21. M. Akbarifar, M. Divandari, On the interfacial characteristics of compound cast Al/brass bimetal. *Inter Metalcast* **11**, 506–512 (2017). <https://doi.org/10.1007/s40962-016-0101-z>
22. Z. Zhang, W. Jiang, G. Li et al., Improved interface bonding of Al/Mg bimetal fabricated by compound casting with Nd addition. *Mater. Sci. Eng. A* **826**, 141998 (2021). <https://doi.org/10.1016/j.msea.2021.141998>
23. M. Akbarifar, M. Divandari, Study of Al/cast iron interface and graphite behavior. *J. Min. Metall. Sect. B* **53**, 53–59 (2017). <https://doi.org/10.2298/JMMB160108027A>
24. M. Sarvari, S. Ghaemi Khiavi, M. Divandari et al., Dissimilar joining of Al/Mg light metals by centrifugal compound casting process. *Inter Metalcast* (2022). <https://doi.org/10.1007/s40962-022-00832-7>
25. E. Hajjari, M. Divandari, S.H. Razavi et al., Inter-metallic compounds and antiphase domains in Al/Mg compound casting. *Intermetallics* **23**, 182–186 (2012). <https://doi.org/10.1016/j.intermet.2011.12.001>
26. E. Hajjari, M. Divandari, S. Razavi et al., Dissimilar joining of Al/Mg light metals by compound casting process. *J. Mater. Sci.* **46**, 6491–6499 (2011). <https://doi.org/10.1007/s10853-011-5595-4>
27. G.X. Wang, E.F. Matthys, Experimental determination of the interfacial heat transfer during cooling and solidification of molten metal droplets impacting on a metallic substrate: effect of roughness and superheat. *Int. J. Heat Mass Transf.* **45**, 4967–4981 (2002). [https://doi.org/10.1016/S0017-9310\(02\)00199-0](https://doi.org/10.1016/S0017-9310(02)00199-0)
28. E. Hajjari, M. Divandari, S.H. Razavi et al., Estimation of the transient interfacial heat flux between substrate/melt at the initiation of magnesium solidification on aluminum substrates using the lumped capacitance method. *Appl. Surf. Sci.* **257**, 5077–5082 (2011). <https://doi.org/10.1016/j.apsusc.2011.01.024>
29. L.A. Jacobson, J. McKittrick, Rapid solidification processing. *Mater. Sci. Eng.* **R11**, 355–408 (1994). [https://doi.org/10.1016/0927-796X\(94\)90022-1](https://doi.org/10.1016/0927-796X(94)90022-1)
30. S. Emami, M. Divandari, H. Arabi et al., Effect of melt-to-solid insert volume ratio on Mg/Al dissimilar metals bonding. *J. Mater. Eng. Perform.* **22**, 123–130 (2013). <https://doi.org/10.1007/s11665-012-0243-y>
31. E. Hajjari, M. Divandari, S. Razavi et al., Microstructure characteristics and mechanical properties of Al 413/Mg joint in compound casting process. *Metall. Mater. Trans. A* **43**, 4667–4677 (2012). <https://doi.org/10.1007/s11661-012-1296-0>
32. X. Daming, J. Limin, F. Hengzhi, Effects of centrifugal and coriolis forces on the mold-filling behavior of titanium melts in vertically rotating molds. *Res. Develop.* (2008). <https://doi.org/10.1016/j.actamat.2011.06.036>
33. M. Gholami, M. Divandari, Interfacial phases and defects characteristics of Al/Cu-Zn bimetal produced via centrifugal casting process. *Iran. J. Mater. Sci. Eng.* **15**, 52–61 (2018)
34. N. Zhang, C. Lei, T. Liu et al., Parameter optimization of Al-5Mg-3Zn-1Cu basin-shaped centrifugal casting: simulation and experimental verification. *Int. J. Metalcast.* (2022). <https://doi.org/10.1007/s40962-022-00822-9>
35. J. Pan, M. Yoshida, G. Sasaki et al., Metal pipe joining with aluminum alloy by ultrasonic insert casting. *Mater. Manuf. Proces.* **15**, 867–881 (2000). <https://doi.org/10.1080/10426910008913027>
36. V. Raghavan, Al-Cu-Zn (aluminum-copper-zinc). *J. Phase Equilib. Diffus.* **28**, 183–188 (2007). <https://doi.org/10.1007/s11669-007-9025-x>
37. S.I. Fujikawa, Interdiffusion between aluminium and α -brass. *Diffus. Mater.* **95–98**, 611–616 (1993). <https://doi.org/10.4028/www.scientific.net/DDF.95-98.611>
38. M. Gholami, M. Divandari, Effect of rotational speeds and heat content on the production of Al-Brass bimetal composite. *J. Sci. Technol. Compos.* **4**, 219–228 (2017)
39. A. Biswas, D.J. Siegel, C. Wolverton et al., Precipitates in Al-Cu alloys revisited: atom-probe tomographic experiments and first-principles calculations of compositional evolution and interfacial segregation. *Acta Mater.* **59**, 6187–6204 (2011). <https://doi.org/10.1016/j.actamat.2011.06.036>
40. B.A. Shoilock, C.R.M. Grovenor, K.M. Knowles, Compositional studies of Ω and Θ' precipitates in an Al-Cu-Mg-Ag alloy. *Scr. Metall.* **24**, 1239–1244 (1990). [https://doi.org/10.1016/0956-716X\(90\)90335-E](https://doi.org/10.1016/0956-716X(90)90335-E)
41. E.I. Marukovich, A.M. Branovitsky, Y.S. Na et al., Study on the possibility of continuous-casting of bimetallic components in condition of direct connection of metals in a liquid state. *Mater. Des.* **27**, 1016–1026 (2006). <https://doi.org/10.1016/j.matdes.2005.02.007>
42. H. Springer, A. Szczepaniak, D. Raabe, On the role of zinc on the formation and growth of intermetallic phases during interdiffusion between steel and

- aluminium alloys. *Acta Mater.* **96**, 203–211 (2015). <https://doi.org/10.1016/j.actamat.2015.06.028>
43. B. Wei, D.M. Herlach, Rapid solidification of undercooled eutectic and monotectic alloys. *Mater. Sci. Eng. A* **173**, 357–361 (1993). [https://doi.org/10.1016/0921-5093\(93\)90244-9](https://doi.org/10.1016/0921-5093(93)90244-9)
 44. X.R. Liu, C.D. Cao, B. Weisheng, Microstructure evolution and solidification kinetics of undercooled Co–Ge eutectic alloys. *Scripta Mater.* **46**, 13–18 (2002). [https://doi.org/10.1016/S1359-6462\(01\)01188-5](https://doi.org/10.1016/S1359-6462(01)01188-5)
 45. J.C. Viala, M. Peronnet, F. Barbeau et al., Interface chemistry in aluminium alloy castings reinforced with iron base inserts. *Compos. Part A* **33**, 1417–1420 (2002)
 46. E. Aguado, A. Baquedano, U. Uribe, et al. Comparative study of different interfaces of steel inserts in aluminium castings. In *Materials Science Forum*; Trans Tech Publ, (2013), pp 711–715. <https://doi.org/10.4028/www.scientific.net/MSF.765.711>
 47. B. Xiong, C. Cai, B. Lu, Effect of volume ratio of liquid to solid on the interfacial microstructure and mechanical properties of high chromium cast iron and medium carbon steel bimetal. *J. Alloy. Compd.* **509**, 6700–6704 (2011). <https://doi.org/10.1016/j.jallcom.2011.03.142>
 48. M.H. Ghoncheh, S.G. Shabestari, M.H. Abbasi, Effect of cooling rate on the microstructure and solidification characteristics of Al2024 alloy using computer-aided thermal analysis technique. *J. Therm. Anal. Calorim.* (2014). <https://doi.org/10.1007/s10973-014-3867-3>
 49. B. Xiong, C. Cai, H. Wan et al., Fabrication of high chromium cast iron and medium carbon steel bimetal by liquid–solid casting in electromagnetic induction field. *Mater. Des.* **32**, 2978–2982 (2011). <https://doi.org/10.1016/j.matdes.2011.01.006>
 50. S. Sarkar, A.K. Lohar, S.C. Panigrahi, Vertical centrifugal casting of aluminum matrix particle reinforced composites. *J. Reinf. Plast. Compos.* **28**, 1013–1020 (2009). <https://doi.org/10.1177/0731684407087757>
 51. M. Abbasi, A. Karimi Taheri, M.T. Salehi, Growth rate of intermetallic compounds in Al/Cu bimetal produced by cold roll welding process. *J. Alloy. Compd.* **319**, 233–241 (2001). [https://doi.org/10.1016/S0925-8388\(01\)00872-6](https://doi.org/10.1016/S0925-8388(01)00872-6)
 52. W.H.S. Lawson, H.W. Kerr, Mechanical behavior of rapidly solidified Al–Al₂Cu and Al–Al₃Ni COMPOSITES. *Metall. Trans.* **2**, 2853–2859 (1971). <https://doi.org/10.1007/BF02813263>
 53. M. Gholami, M. Divandari, M.T. Salehi, Experimental study of effective parameters on production and mechanical properties of Al–brass bimetal composite. *Modares Mech. Eng.* **16**, 170–178 (2016)
 54. C.D. Beachem, The effects of crack tip plastic flow directions upon microscopic dimple shapes. *Metall. Trans. A* **6**, 377–383 (1975). <https://doi.org/10.1007/BF02667293>
 55. A. Gilbert, G.T. Hahn, C.N. Reid et al., Twin-induced grain boundary cracking in bcc metals. *Acta Metall.* **12**, 754 (1964)
 56. J.X. Zhou, X. Shen, Y.J. Yin et al., Gas-liquid two phase flow modelling of incompressible fluid and experimental validation studies in vertical centrifugal casting. *Mater. Sci. Eng.* (2015). <https://doi.org/10.1088/1757-899X/84/1/012042>
 57. J. Zhang, J.X. Zhou, M. Zhang et al., Numerical simulation of filling process in vertical centrifugal casting based on projection-level set method. *Adv. Mater. Res.* **314–316**, 364–368 (2011). <https://doi.org/10.4028/www.scientific.net/AMR.314-316.364>
 58. E. Trejo, *Centrifugal casting of an aluminium alloy* (University of Birmingham, 2011)
 59. L.L. Regel, W.R. Wilcox, Centrifugal materials processing. *Int. Center Gravity Mater. Sci. Appl.* (1997). https://doi.org/10.1007/978-1-4615-5941-2_1
 60. W. Shi-ping, L. Chang-yun, G.U. Jing-jie et al., Numerical simulation and experimental investigation of two filling methods in vertical centrifugal casting. *Trans. Nonferrous Met. Soc. China* **16**, 1035–1040 (2006). [https://doi.org/10.1016/S1003-6326\(06\)60373-7](https://doi.org/10.1016/S1003-6326(06)60373-7)
 61. Q. Dong, Z. Yin, H. Li et al., Simulation study on filling and solidification of horizontal centrifugal casting babbitt lining of bimetallic bearing. *Int. J. Metalcast.* **15**, 119–129 (2021). <https://doi.org/10.1007/s40962-020-00429-y>

Publisher’s Note Springer Nature remains neutral with regard to jurisdictional claims in published maps and institutional affiliations.

Springer Nature or its licensor (e.g. a society or other partner) holds exclusive rights to this article under a publishing agreement with the author(s) or other rightsholder(s); author self-archiving of the accepted manuscript version of this article is solely governed by the terms of such publishing agreement and applicable law.